

IR²QSM: Quantitative Susceptibility Mapping via Deep Neural Networks with Iterative Reverse Concatenations and Recurrent Modules

Min Li, Chen Chen, Zhuang Xiong, Ying Liu, Pengfei Rong, Shanshan Shan, Feng Liu, Hongfu Sun, Yang Gao*

Abstract—Quantitative susceptibility mapping (QSM) is an MRI phase-based post-processing technique to extract the distribution of tissue susceptibilities, demonstrating significant potential in studying neurological diseases. However, the ill-conditioned nature of dipole inversion makes QSM reconstruction from the tissue field prone to noise and artifacts. In this work, we propose a novel deep learning-based IR²QSM method for QSM reconstruction. It is designed by iterating four times of a reverse concatenations and middle recurrent modules enhanced U-net, which could dramatically improve the efficiency of latent feature utilization. Simulated and *in vivo* experiments were conducted to compare IR²QSM with several traditional algorithms (MEDI and iLSQR) and state-of-the-art deep learning methods (U-net, xQSM, and LPCNN). The results indicated that IR²QSM was able to obtain QSM images with significantly increased accuracy and mitigated artifacts over other methods. Particularly, IR²QSM demonstrated on average the best NRMSE (27.59%) in simulated experiments, which is 15.48%, 7.86%, 17.24%, 9.26%, and 29.13% lower than iLSQR, MEDI, U-net, xQSM, LPCNN, respectively, and led to improved QSM results with fewer artifacts for the *in vivo* data.

Index Terms—QSM, Dipole inversion, IR²QSM, Reverse Concatenation, Recurrent Module

I. INTRODUCTION

Quantitative Susceptibility Mapping (QSM) is a post-processing technique to extract the distribution of tissue susceptibilities from the MRI phases [1-4]. QSM has shown significant potential in investigating various neurodegenerative diseases [5-11], alcohol use disorder [12], healthy aging [13-17] and intracranial hemorrhage [18-20]. Furthermore, it has been utilized in studies of brain function by measuring variations in brain oxygen levels [21-23]. However, QSM reconstruction typically involves several non-trivial intermediate processing

steps. First, phase unwrapping should be conducted to remove the phase wraps in MRI phases. Then, a background field removal step is carried out to extract the so-called local field maps from the unwrapped phases. Finally, QSM images are reconstructed via dipole inversion from the local field, which is inherently an ill-posed inverse problem.

There have been many efforts devoted to solving the QSM dipole inversion. The COSMOS method (Calculation Of Susceptibility through Multiple Orientation Sampling) [24] has long been considered a gold standard for QSM reconstruction outside the anisotropic white matter regions. However, this method requires at least three repetitive MRI scans at different head orientations, which is very time-consuming and requires the patients to rotate their heads accordingly, making this method impractical for clinical applications. For the single-orientation QSM, TKD [25] mitigates small dipole kernel values by thresholding, but often causes streaking artifacts and estimation errors. Therefore, some other traditional methods, e.g., iLSQR [26], MEDI [27, 28], SFCR [29], STAR-QSM [30], and LN-QSM [31], have been proposed to solve high-quality QSM images from single-orientation local field maps. However, these methods are usually computationally intensive and need manual parameter tuning for different data.

Recently, deep neural networks have become increasingly popular for solving QSM dipole inversion problems. QSMnet [32] was the first to train a U-net to produce COSMOS-like images from single-orientation local field maps, which was then evolved to QSMnet+ [33] by taking advantage of the data augmentation strategy. QSMGAN [34], LPCNN [35], S2Q-Net [36], and MoDL-QSM [37] further improved this training framework (taking *in vivo* acquired local field data as network inputs, and using QSM images reconstructed by traditional methods as labels) by more sophisticated network designs. Alternatively, DeepQSM [38] and xQSM [39] proposed to use

This work was supported by the National Natural Science Foundation of China under Grant No. 62301616 and 62301352, the Natural Science Foundation of Hunan under Grant No. 2024JJ6530, Hunan Provincial Science and Technology Program (NO.2021RC4008), and the HighPerformance Computing Center of Central South University. HS thanks the support from the Australia Research Council (DE20101297 and DP230101628). Correspondence: Yang Gao (yang.gao@csu.edu.cn), Room 429, Information Building, Central South University, Changsha, China.

Min Li, Chen Chen, and Yang Gao are with the School of Computer Science and Engineering, Central South University, Changsha, China.

Zhuang Xiong and Feng Liu are with the School of Electrical Engineering and Computer Science, University of Queensland, Brisbane, Australia.

Yin Liu and Pengfei Rong are with the Department of Radiology, The Third Xiangya Hospital, Central South University, Changsha, China.

Hongfu Sun is with School of Engineering, University of Newcastle, Newcastle, Australia.

Shanshan Shan is with State Key Laboratory of Radiation, Medicine and Protection, School for Radiological and Interdisciplinary Sciences (RAD-X), Collaborative Innovation Center of Radiation Medicine of Jiangsu Higher Education Institutions, Soochow University, Suzhou, China.

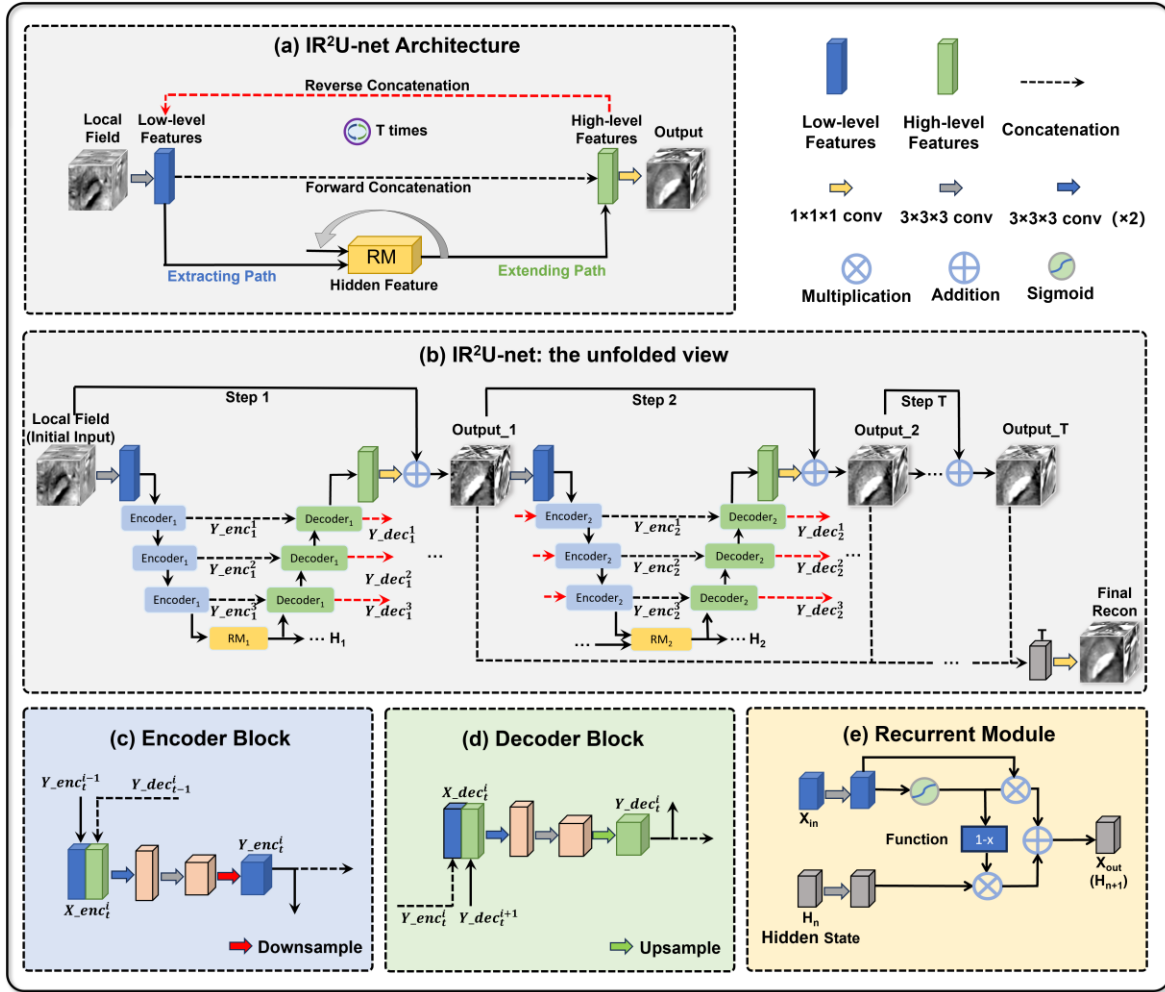


Fig. 1. Overview of the proposed IR²QSM trained from the proposed (a) IR²U-net. (b) depicts the detailed and unrolled view of IR²U-net, which is implemented by iterating a specially tailored U-net for T times. In addition to the conventional (c) Encoder and (d) Decoder blocks, three Reverse Concatenations (the dashed red line at the top of (a)) and one (e) middle Recurrent Module module are also introduced in the U-net to enhance the efficiency of the latent feature utilization.

pure synthetic or simulated training datasets (generated using the dipole forward model [38]) for deep neural network training, so that their training inputs and labels satisfy the underlying physical model. SAQSM [40] proposed using spatial adaptive modules to reduce susceptibility information loss. AFTER-QSM [41] and MoDIP-QSM [42] could reconstruct QSM images from local field data acquired at different acquisition resolutions and orientations. AdaIN-QSM [43] was capable of resolution-agnostic reconstruction. In addition to these networks for dipole inversion, autoQSM [44] could reconstruct QSM from the total field maps, while iQSM and iQSM+ [45, 46] could extract QSM from the raw wrapped phases in a single step.

Although deep learning techniques have shown promising results in QSM reconstruction, nearly all existing methods were implemented on simple U-nets. In this work, we would like to propose a novel IR²QSM method for dipole inversion via training a specially designed new baseline network, i.e., IR²U-net, on a simulated brain dataset. The proposed IR²U-net is constructed by Iterating a Reverse concatenation and Recurrent module enhanced U-net four times. Three reverse concatenations from the U-net’s extended path to the extracted

path were incorporated to fully refine the latent features, and a middle recurrent module was designed for efficient and effective capturing of long-distance information, considering the non-local nature of QSM reconstruction. Comparative experiments on simulated brains, public QSM challenge data, *in vivo* healthy volunteers, and pathological data were conducted to investigate the performances of the proposed IR²QSM with several established QSM dipole inversion methods, including traditional iLSQR, MEDI, and deep learning (DL) based U-net, xQSM, and LPCNN methods.

II. METHOD

A. QSM Dipole Inversion

The relationship between the susceptibility χ and tissue phase φ is a convolution with a dipole kernel in the spatial domain, which can be represented by the following equation in k-space [47, 48]:

$$\varphi(\vec{r}) = F^{-1}D(\vec{k}) \cdot F\chi(\vec{r}), \quad (1)$$

where \vec{r} and \vec{k} are the spatial domain and k-space coordinates respectively; F is the Fourier transform; “ \cdot ” denotes the

element-wise multiplication, and $D(\vec{k})$ represents the dipole kernel in the k-space, which can be expressed as the following equation (at pure axial acquisition):

$$D(\vec{k}) = \frac{1}{3} - \frac{k_z^2}{k_x^2 + k_y^2 + k_z^2}, \quad (2)$$

Note that the dipole kernel has a zero-valued double-conical surface ($k_x^2 + k_y^2 = 2k_z^2$) in k-space, making the QSM dipole inversion an ill-posed problem. Equation (1) was also used as the training data generator in many previous DLQSM methods [38, 39, 41].

B. Network Architecture

1) Overall Structure

The proposed IR²QSM was trained on a novel network backbone, Iterating **R**everse concatenations and **R**ecurrent modules enhanced **U**-net (IR²U-net), on a simulated dataset. Overall, the proposed IR²U-net is constructed by iterating T times of a specially tailored U-net (Fig. 1(a)), which is designed by inserting reverse concatenation (RC) connections from the expanding to extracting path and a middle recurrent module (RM) into a conventional U-net. The RC and RM designs are beneficial for efficiently processing long-distance information, which helps enhance the non-local QSM dipole inversion.

Figure 1(b) illustrates the unfolded view of the proposed IR²U-net, which can be seen as T -cascading U-nets enhanced with the proposed RC and RM modules. As demonstrated in Fig. 1(c) and (d), each encoder or decoder block in the U-net consists of 2 convolutional layers (3^3 kernel size with stride 1), 2 batch normalization layers, and 2 rectified linear units (ReLU), followed by 1 max-pooling layer (2^3 kernel size with stride 1) or 1 transposed convolution layer (2^3 kernel size with stride 1), respectively. Like conventional U-nets, the upsampling and downsampling data flow enable the network to process multi-scale information by scaling the feature map to different image resolutions. The middle RM module (Fig. 1(e)) is composed of 2 convolutional layers (3^3 kernel size with stride 1), 2 batch normalization layers, and 2 ReLUs.

The proposed IR²U-net will produce T latent output images during the T iterative steps. In this work, all these latent outputs are concatenated channel-wisely and fed into a final convolution layer (1^3 kernel size with stride 1) to obtain the final output (i.e., the QSM reconstruction), as shown in the center part of Fig. 1(b). In this work, the intermediate U-nets are independent of each other (they are not sharing the same parameters), and we empirically set $T=4$, taking both the performances and computational costs into consideration.

2) Reverse Concatenation

As we have described above, the IR²U-net can be interpreted as T cascading U-nets with three encoders and decoders. Suppose that the input and output feature maps of the i^{th} encoder block in the i^{th} intermediate U-net are denoted by $X_{enc_t}^i$ and $Y_{enc_t}^i$, respectively, while the features from the corresponding decoder block are denoted by $X_{dec_t}^i$ and $Y_{dec_t}^i$. Then, the RC connections can be described as follows:

$$\begin{aligned} X_{enc_t}^i &= \text{Concat}(Y_{enc_t}^{i-1}, Y_{dec_t}^{i-1}) \\ Y_{dec_t}^i &= \Psi_{dec}(X_{dec_t}^i), \end{aligned} \quad (3)$$

$$Y_{enc_t}^i = \Psi_{enc}(X_{enc_t}^i)$$

where Ψ_{enc} and Ψ_{dec} denote the cascading operations in the encoder/decoder blocks (2 convolution + 2BN + 2ReLU + max-pooling or transposed convolution). The input to the encoder blocks ($X_{enc_t}^i$) is dependent on both the latent features of the current time step ($X_{enc_t}^{i-1}$) and the previous time step ($X_{dec_{t-1}}^i$), forming a reverse data flow from the high-level features to the low-level features of the proposed backbone, as illustrated in Fig. 1(a).

3) Recurrent Module

As shown in Fig. 1(e), the RM module is inspired by the architecture of Recurrent Neural Networks (RNNs) [49-51]. Suppose that the input of the RM block (the t^{th} intermediate U-net) is X_t , and the hidden state from the previous iterations is represented by H_{t-1} . Then, the RM can be described as Eq. (4):

$$\alpha = \text{sigmoid}(\text{Conv3D}(X_t)) \quad (4)$$

$Y_t = \text{Conv3D}(X_t) * \alpha + \text{Conv3D}(H_{t-1}) * (1 - \alpha)$, where Y_t represents the output of the current RM module and is also cached as H_t , i.e., the hidden state feature for the $t+1^{\text{th}}$ module, and in the first RM module, we set $H_0 = X_1$.

C. Network Training

All network parameters were initialized using random numbers of a normal distribution with a mean of 0 and a standard deviation of 0.01. All networks were trained for 100 epochs on one Nvidia Tesla A6000 GPU for 60 hours, using the Adam optimizer. The learning rate was set to 10^{-3} for the first 30 epochs, 10^{-4} for epochs 30 to 60, and 10^{-5} for the final 40 epochs; all other hyperparameters were set to their default values. Pretrained IR²QSM networks and related codes can be found at: <https://github.com/YangGaoUQ/IR2QSM>.

Furthermore, a recently proposed noise-adding module [39] was incorporated during network training to improve the network's performance on the *in vivo* dataset. 5% connections in each layer of the proposed network were also randomly dropped out for better generalization capability, more details about this choice can be found in the Discussion Section (Section V). Note that the noise-adding block and dropout were only added during network training and removed during network inference.

The loss function for the network training in this work consists of two parts:

$$L = \sum_{t=1}^T \omega_t \text{MSE}(\chi_t, \chi_{GT}) + \text{MSE}(\chi_{final}, \chi_{GT}), \quad (5)$$

where χ_t represents the output of the t^{th} intermediate U-net in Fig. 1(b), χ_{final} is the final IR²QSM reconstruction, and χ_{GT} is the training ground truth. $\omega_t = \lambda^{T-t}$ is the weighting parameters between different various loss terms, and we empirically set λ as 0.5 in this work.

III. EXPERIMENTAL SETUP

A. Training Data Preparation

A total of 14,400 three-dimensional QSM patches (size: 64^3) were cropped from 96 full-sized QSM volumes (image size: $144 \times 196 \times 128$) by traversing the full-sized volumes with a stride of $24 \times 36 \times 20$ for network training. The full-sized data

were acquired at 3T with 1 mm isotropic resolution and reconstructed using traditional algorithms, i.e., best-path [52] for phase unwrapping, RESHARP [53] for background removal, and iLSQR [26] for dipole inversion. Similar to xQSM [39] and DeepQSM [38], the IR²QSM was trained on simulated datasets generated with Equation (1).

B. Evaluation Dataset and Comparative Experiments

In this work, the proposed IR²QSM was compared with two iterative algorithms, i.e., iLSQR [26] and MEDI [27], and three deep learning methods, i.e., the U-net, xQSM [39], and LPCNN[35], on both simulated and *in vivo* human brain subjects.

First, 10 brain data were simulated from a publicly available COSMOS label [24] (matrix size: 216×224×160) at 3T with 1 mm isotropic resolution to investigate the effects of the overall network iteration number T , RC, and RM on IR²QSM results respectively.

Then, we quantitatively compared the proposed IR²QSM with traditional and deep learning QSM methods using Normalized Root Mean Square Error (NRMSE), High-Frequency Error Norm (HFEN) [8], and Structural Similarity Index (SSIM) [44] on another COSMOS-based simulated data at 3T (1mm isotropic resolution, matrix size: 192×256×176) generated using Eq. (1) and two synthesized data from the 2019 QSM Reconstruction Challenge 2.0 [54] (<http://qsm.snu.ac.kr/?pageid=30>).

We also quantitatively compared the susceptibility measurements of the proposed IR²QSM with other QSM methods in five deep grey matter regions, including Globus Pallidus (GP), Putamen (PU), Caudate (CN), Substantia Nigra (SN), and Red Nucleus (RN) on a simulated COSMOS brain.

In addition, the performance of IR²QSM was also validated on four *in vivo* datasets:

(1) A healthy brain data acquired at 3T with the following acquisition parameters: 8 unipolar echoes, matrix size: 256×256×128, 1 mm isotropic resolution, First TE / Δ TE / TR = 3 / 3.3 / 29.8 ms.

(2) A cerebral amyloid angiopathy (CAA) patient was scanned at 3T. The parameters are: 10 unipolar echoes, matrix size = 224×224×128, 1 mm isotropic resolution, First TE / Δ TE / TR = 4.2 / 4.1 / 43.4 ms.

(3) A patient with intracranial hemorrhage (ICH) scanned at 3T, with the following parameters: 7 unipolar echoes, matrix size: 180×224×144, 1 mm isotropic resolution, First TE / Δ TE / TR = 4.79 / 4.80 / 40 ms.

(4) A multiple sclerosis (MS) patient scanned at 3T, using the following parameters: 7 unipolar echoes, matrix size: 256×256×128, 1 mm isotropic resolution, First TE / Δ TE / TR = 4.79 / 4.80 / 40 ms.

IV. RESULTS

A. The Effects of The Overall Iteration Number T

The influences of the overall iteration number T in the proposed IR²QSM were investigated using 10 simulated brains, and the evaluation metrics were summarized in Table I. Increasing iteration number T from 1 to 4 was effective in improving IR²QSM's reconstruction accuracy, and led to on average 24.89% reduction in NRMSE, 19.43% reduction in HFEN, and 2.58% increase in SSIM. However, it is also found that $T=5$ did not led to much more improvements, the computational cost went higher as the T increased, and therefore, in this work, we empirically set $T=4$, taking both the network's performances and the computational costs into consideration. Note that in the following sections of the paper,

TABLE I
THE INFLUENCES OF OVERALL ITERATION NUMBER T ON IR²QSM RESULTS

METHOD	NRMSE(%)	HFEN(%)	SSIM(%)	TIME	GfLOPS
				CPU(S)	
	MEAN \pm STD				
$T=1$	52.48 \pm 0.857	39.16 \pm 0.450	96.23 \pm 0.162	3.85	34.81
$T=2$	38.04 \pm 0.298	30.11 \pm 0.361	97.35 \pm 0.151	8.36	75.99
$T=3$	30.04 \pm 0.648	21.38 \pm 0.262	98.58 \pm 0.069	12.58	117.17
$T=4$	27.59 \pm 0.455	19.73 \pm 0.346	98.81 \pm 0.055	16.87	158.35
$T=5$	27.78 \pm 0.389	19.84 \pm 0.522	98.82 \pm 0.087	21.38	199.53

all the IR²QSM reconstructions, if not specified, are the results of 4 iteration numbers.

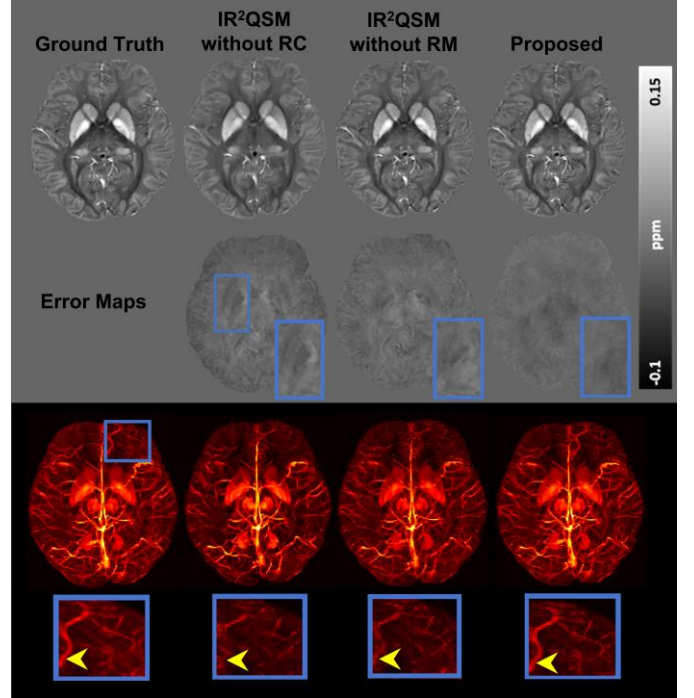


Fig. 2. The effectiveness of the proposed recurrent module (RM) and reverse concatenation (RC) on IR²QSM results. The top two rows show the IR²QSM reconstructions with the corresponding error maps relative to the ground truth; the bottom two rows illustrate the maximum Intensity Projection (mIP) results. Yellow arrows point to a blurry vein in IR²QSM without RC or RM.

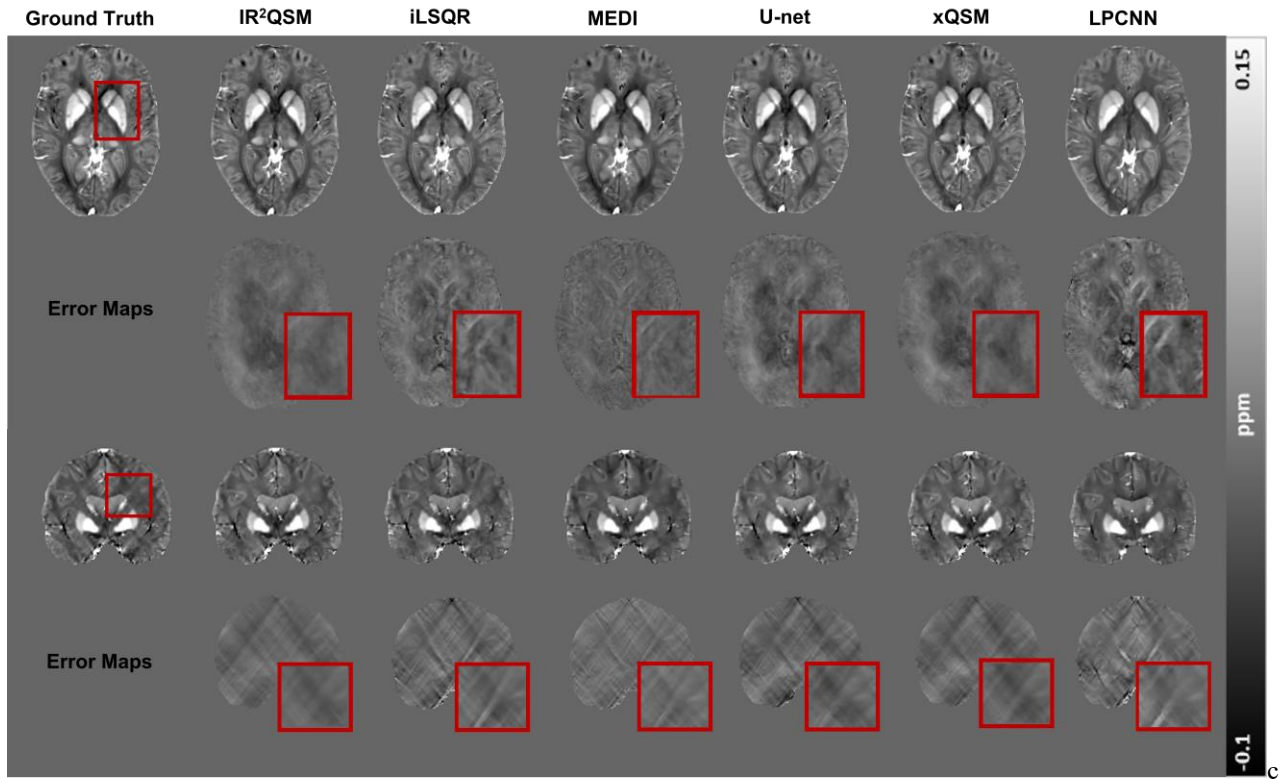


Fig. 3. Comparison of IR²QSM with various QSM methods on a COSMOS-based simulated brain at 3T on two orthogonal planes. Error maps from the zoomed-in regions as highlighted by the red boxes are amplified.

B. Ablation Study on Recurrent Modules and Reverse Concatenations

An ablation study was also conducted on a simulated brain at 3T to examine the effects of the proposed recurrent module (RM) and reverse concatenation (RC) connections in IR²QSM, and the results are shown in Fig. 2. According to the difference maps and the maximum Intensity Projection (mIP) images, both the RM and the RC designs are effective and could significantly enhance the reconstruction results, as highlighted in the zoom-in error maps and the vessel in mIP (yellow arrows).

The numerical metrics on the simulated brains are reported in Table II. The performances of IR²QSM without RM or RC dramatically dropped, e.g., NRMSE on average increased from 27.59% to 29.56% and 35.81%, which may also implicit that the RC design contributed more than RM (6.25% improvements in NRMSE).

C. Comparative Studies on Simulation Data

1) COSMOS-Based Simulated Brain Data Results.

Different QSM methods were compared using a COSMOS-

based simulated brain (3T, 1 mm isotropic) in Fig. 3. IR²QSM showed the best reconstruction results with visually minimum error maps, and the corresponding numerical metrics (NRMSE, HFEN, and SSIM) were reported in Table III. For instance, the NRMSE of IR²QSM is 27.59%, compared to 43.07%, 35.45%, 44.83%, 36.85%, and 56.72% of iLSQR, MEDI, U-net, xQSM, and LPCNN, respectively.

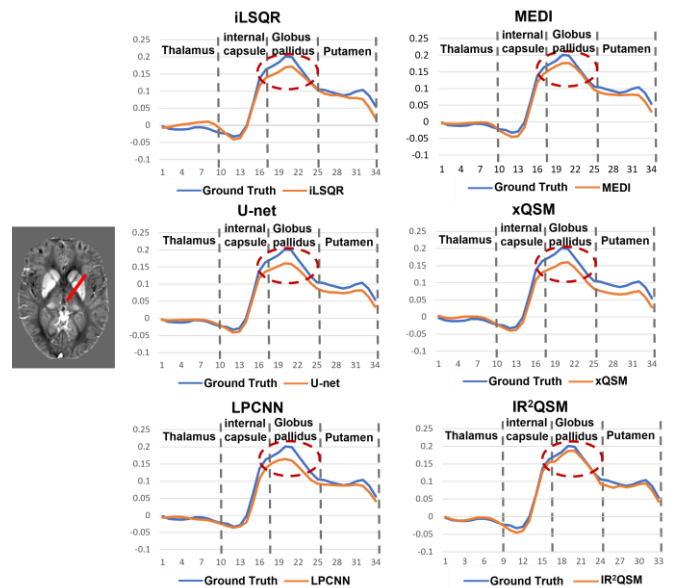


Fig. 4. Susceptibility measurements of different QSM methods on the red line in the deep grey matter regions. Red circles highlight the differences between various QSM results and the ground truth.

TABLE II
ABLATION STUDY OF IR²QSM ON THE EFFECTS OF REVERSE CONCATENATION OR RECURRENT MODULE USING TEN SIMULATED BRAINS

METHOD	NRMSE(%)	HFEN(%)	SSIM(%)
IR ² QSM without RM	29.56 \pm 0.633	21.30 \pm 0.345	98.54 \pm 0.067
IR ² QSM without RC	35.81 \pm 0.512	26.96 \pm 0.201	97.83 \pm 0.112
IR ² QSM (Proposed)	27.59 \pm 0.455	19.73 \pm 0.346	98.81 \pm 0.055

TABLE III
COMPARISON OF VARIOUS QSM RESULTS ON A COSMOS-BASED SIMULATED BRAIN

METHOD	NRMSE(%)	HFEN(%)	SSIM(%)
		MEAN \pm STD	
iLSQR	43.07 \pm 1.404	40.46 \pm 0.665	96.21 \pm 0.201
MEDI	35.45 \pm 1.133	31.18 \pm 0.384	96.05 \pm 0.203
U-net	44.83 \pm 0.641	34.72 \pm 0.326	96.51 \pm 0.184
xQSM	36.85 \pm 0.739	26.18 \pm 0.388	97.89 \pm 0.113
LPCNN	56.72 \pm 0.563	53.42 \pm 0.421	92.95 \pm 0.299
IR ² QSM	27.59 \pm 0.455	19.73 \pm 0.346	98.81 \pm 0.055

Figure 4 compares the susceptibility profiles of different QSM methods along the red line crossing several deep grey matter regions (thalamus (TH), internal capsule (IC), GP, and PU). IR²QSM demonstrated the closest susceptibility measurements compared with the simulation ground truth (highlighted with red circles).

2) 2019 QSM Challenge 2.0 Dataset Results

The proposed IR²QSM was compared with various QSM methods using the 2019 QSM challenge 2.0 dataset in Fig. 5. MEDI led to the minimum error maps for contrast "SIM1" (top two rows), while IR²QSM was overall the best DLQSM method and led to the best SSIM for both contrasts and the best HFEN for contrast "SIM2" (bottom two rows) among all algorithms, as confirmed by Table IV.

TABLE IV
COMPARISON OF VARIOUS QSM METHODS ON 2019 QSM CHALLENGE 2.0 DATASET.

METHOD	NRMSE(%)	HFEN(%)	SSIM
		SIM1/SIM2	
iLSQR	69.34/60.27	52.31/53.28	0.918/0.982
MEDI	53.61/50.69	39.26/49.47	0.960/0.991
U-net	68.13/67.67	47.20/52.04	0.970/0.990
xQSM	66.75/62.95	43.07/47.30	0.973/0.990
LPCNN	56.50/56.98	52.23/57.53	0.898/0.990
IR ² QSM	64.48/58.23	39.57/ 38.80	0.981/0.991

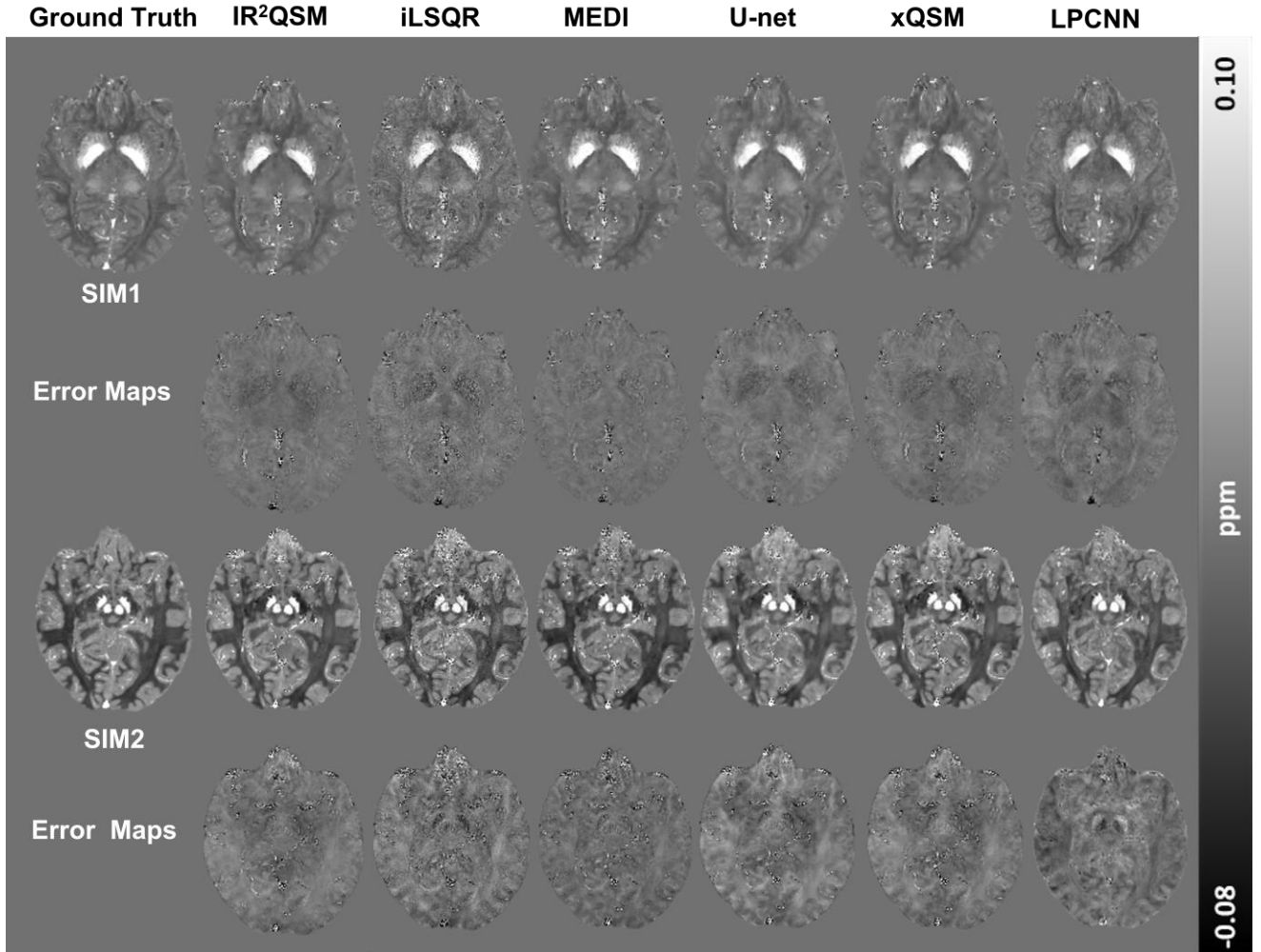


Fig. 5. Comparison of different dipole inversion methods on the 2019 QSM Challenge 2.0 data. The top two rows show the QSM images and corresponding error maps for data "SIM1", while the bottom two rows depict the results and error maps for data "SIM2".

3) Susceptibility Measurements Analysis in Five DGM Regions

Figure 6 compares susceptibility measurements of different QSM methods in five DGM regions using linear regression. IR²QSM achieved the highest accuracy relative to the ground truth in GP, CN, and RN regions with fitting slopes of 0.94, 0.95, and 0.97, respectively. In particular, in the CN region, the fitting slope of IR²QSM is 0.95, and that of iLSQR, MEDI, UNet, xQSM, and LPCNN is 0.87, 0.91, 0.85, 0.91, 0.87, respectively. In addition, IR²QSM also demonstrated minimum mean squared errors (MSE) in GP, PU, and CN regions and the highest coefficient of determination (R^2) in PU and CN regions, as detailed in Table V.

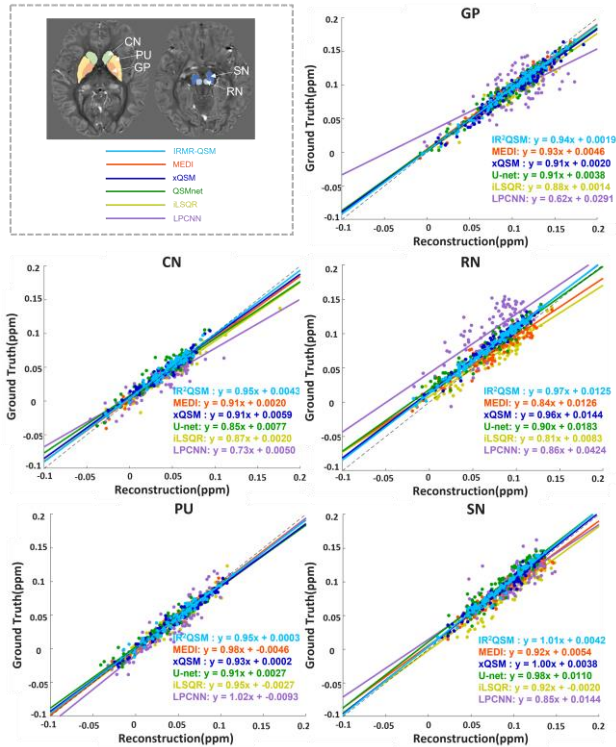


Fig. 6. Scatter plots of susceptibility measurements in five deep grey matter regions of various QSM methods (x-axis) against the ground truth (y-axis). Linear regression results are reported correspondingly.

D. In Vivo Healthy Subjects

Figure 7 compares IR²QSM with other QSM methods on an *in vivo* brain acquired at 3T. IR²QSM showed comparable results with COSMOS and other existing QSM dipole inversion methods in deep grey matter regions, as highlighted in the zoomed-in images in Fig. 7(a). The susceptibility measurements of five DGM were also quantitatively compared in Fig. 7(b). Statistical *t*-tests (carried out based on all voxels inside the ROIs) found that IR²QSM led to similar quantitative measurements in GP compared to COSMOS, while iLSQR, MEDI, and U-net exhibited significantly underestimated results, on average 0.024 ($P=0.003$), 0.019 ($P=0.015$), and 0.012 ($P=0.028$) ppm lower, respectively.

E. In Vivo Pathological Brain Data

Figure 8 compares the proposed IR²QSM results with iLSQR,

TABLE V
QUANTITATIVE ANALYSIS OF SUSCEPTIBILITY MEASUREMENTS RESULTS IN FIVE DGM REGIONS.

METHOD	GP	PU	CN	RN	SN
iLSQR	19.90/0.880	8.17/0.967	7.48/0.960	14.67/0.948	19.36/0.890
MEDI	4.44/ 0.990	2.99/0.995	3.74/0.988	11.87/0.972	5.969/ 0.992
U-net	10.92/0.963	4.80/0.989	8.32/0.975	22.37/0.885	17.93/0.890
xQSM	11.36/0.942	4.26/0.985	4.08/0.986	15.89/0.893	4.78/0.986
LPCNN	65.79/0.784	28.72/0.914	22.06/0.852	162.8/0.105	27.46/0.977
IR ² QSM	4.43/0.979	2.61/0.995	2.86/0.991	12.21/0.914	5.19/0.963

MEDI, U-net, xQSM, and LPCNN using three *in vivo* pathological subjects. All methods successfully detected the pathological lesions in all three brains; however, iLSQR, MEDI, and LPCNN led to more artifacts in the sinus region, as highlighted by the yellow arrows. In addition, LPCNN also presented over-smoothing results with suppressed contrasts.

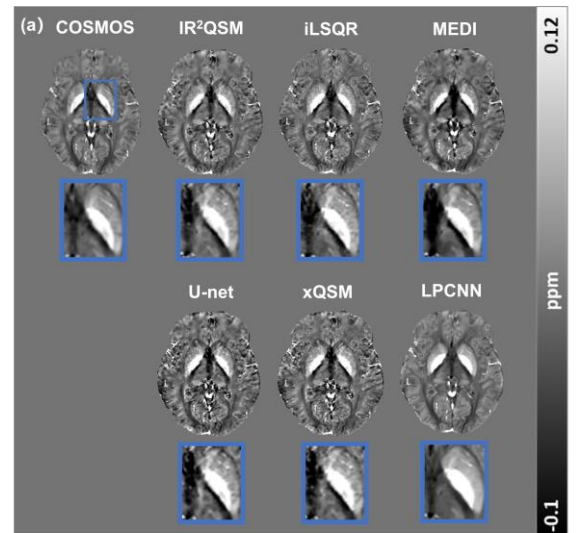


Fig. 7. Comparison of various QSM methods on an *in vivo* subject acquired at 3T. (a) shows the QSM results of different methods, and the bar graphs in (b) compare the susceptibility measurements of IR²QSM with other QSM methods in five DGM regions.

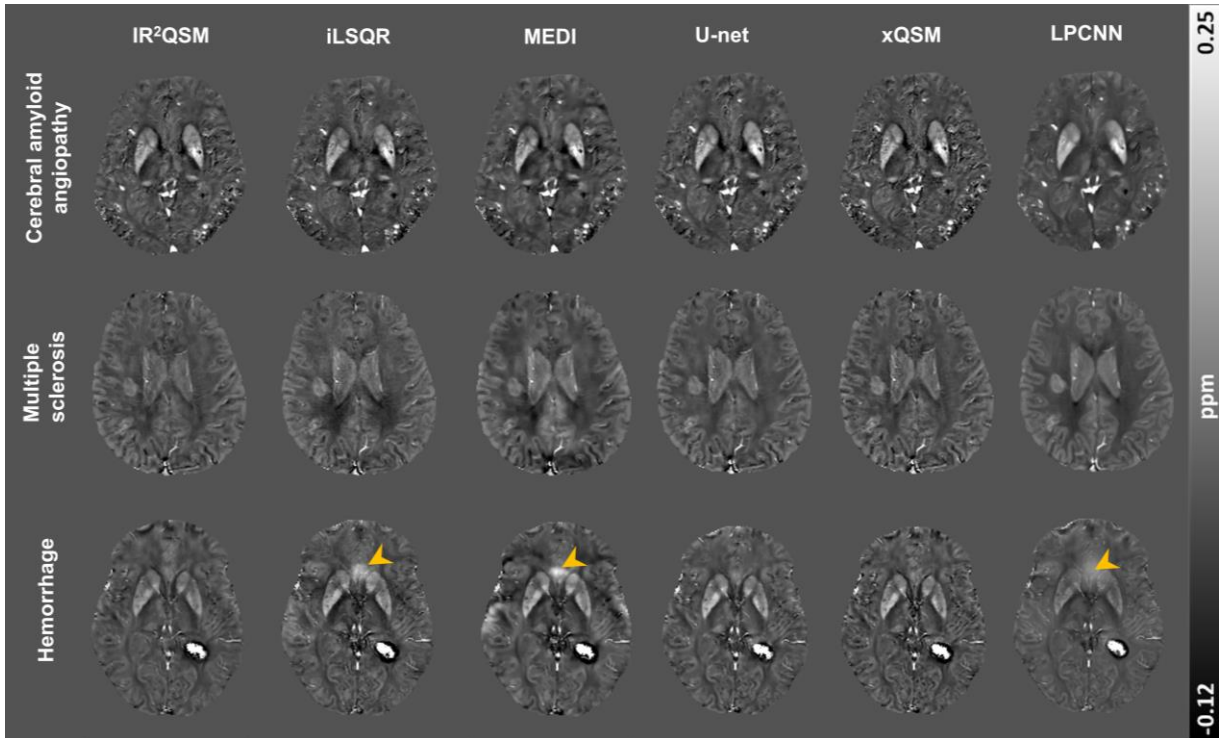


Fig. 8. Comparison of IR²QSM with various QSM methods on three *in vivo* pathological brain data from patients with cerebral amyloid angiopathy, multiple sclerosis, and intracranial hemorrhage, respectively. Yellow arrows point to the artifacts in iLSQR, MEDI, and LPCNN methods.

V. DISCUSSION

In this study, we proposed a new DLQSM dipole inversion method, namely IR²QSM, which was trained on our proposed IR²U-net on a simulated training dataset. The novel IR²U-net was constructed by iterating four times of a specially tailored U-net, which is empowered by Reverse Concatenations and Recurrent Modules. IR²QSM was compared with two traditional and several state-of-the-art deep learning methods (i.e., iLSQR, MEDI, U-net, xQSM, LPCNN) using a comprehensive brain dataset, including both simulated and *in vivo* brains. It showed the best numerical performances (e.g.,

NRMSE, HFEN, and SSIM) on the simulated brains and also presented QSM images with the least noise and artifacts on the *in vivo* dataset, and in the meantime, it successfully alleviated the over-smoothing and susceptibility underestimation in LPCNN results.

The key designs in the proposed IR²QSM are the Reverse Concatenations (RC) and Recurrent Modules (RM). With the help of RCs from the U-net’s expanding path to the extracting path, the network could efficiently merge high-level semantic features with low-level semantic features. Meanwhile, the RM facilitated long-distance information processing with an RNN-like recursive design. Overall, these two modules resulted in

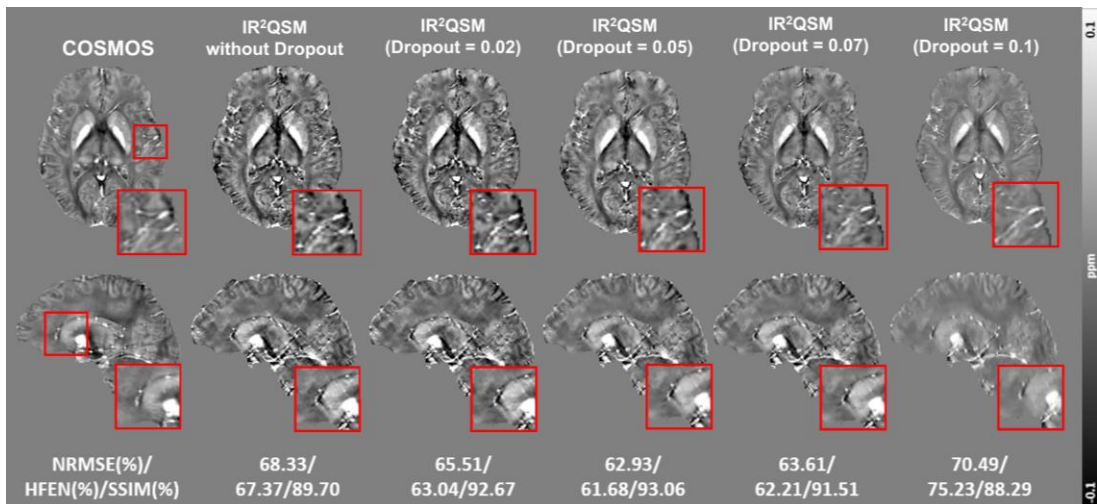


Fig. 9. The influences of dropout rate during network training on IR²QSM results on a healthy subject acquired at 3T. Quantitative numerical metrics between the reconstructed images and a COSMOS reference are also reported correspondingly.

dramatically improved numerical metrics, as demonstrated in the ablation studies.

As reported in a previous review paper [55], DLQSM methods trained on simulated or synthesized datasets are more prone to noise and artifacts in the *in vivo* subjects. To alleviate this problem in IR²QSM, in addition to our previously proposed noise-adding layer in xQSM, we also adopted the dropout technique [56, 57] during network training to improve IR²QSM generalization capability. Figure 9 compares IR²QSM trained without and with dropout (at 0.02, 0.05, 0.07, 0.1 rates) on an *in vivo* data acquired at 3T. The results indicated that dropping out an appropriate proportion (i.e., 0.02, 0.05, and 0.07) of the network connections during network training was very effective in mitigating the noise and artifacts in the *in vivo* data, compared with IR²QSM results without any dropout. However, relatively higher dropout rates (0.1) could lead to significant over-smoothing in the QSM results, and in this work, we manually set a 0.05 rate as our final choice, which also led to the most similar results to the COSMOS reference, with the best NRMSE/HFEN/SSIM metrics.

In this work, although IR²QSM showed improved results compared with previous DLQSM methods, i.e., U-net, xQSM, and LPCNN, the computational loads (e.g., the FLOPs and reconstruction speeds) of IR²QSM also dramatically increased, which could be a drawback in speed-demanding applications. Additionally, we limited our experiments to human brain data acquired with 1 mm isotropic resolution (consistent with the training data) only, and in the future, more comprehensive tests of different resolutions or subjects beyond human brains should be carried out to further validate the proposed method. Future work will also investigate more advanced network backbones for faster and more precise DLQSM reconstruction in the meantime.

VI. CONCLUSION

In this work, we proposed a novel IR²QSM method for QSM dipole inversion and conducted comparative experiments based on a comprehensive dataset including both simulated brains and *in vivo* subjects. The results demonstrated that IR²QSM led to results with better numerical metrics and improved robustness to noise and artifacts, compared with multiple established traditional and deep learning methods.

REFERENCES

- [1] L. de Rochefort, R. Brown, M. R. Prince, and Y. Wang, "Quantitative MR susceptibility mapping using piece-wise constant regularized inversion of the magnetic field," *Magn Reson Med*, vol. 60, no. 4, pp. 1003-9, Oct 2008.
- [2] C. Langkammer, F. Schweser, N. Krebs, A. Deistung, W. Goessler, E. Scheurer, K. Sommer, G. Reishofer, K. Yen, F. Fazekas et al., "Quantitative susceptibility mapping (QSM) as a means to measure brain iron? A post mortem validation study," *Neuroimage*, vol. 62, no. 3, pp. 1593-1599, 2012.
- [3] C. Liu, H. Wei, N. J. Gong, M. Cronin, R. Dibb, and K. Decker, "Quantitative Susceptibility Mapping: Contrast Mechanisms and Clinical Applications," *Tomography*, vol. 1, no. 1, pp. 3-17, Sep 2015.
- [4] Y. Wang and T. Liu, "Quantitative susceptibility mapping (QSM): Decoding MRI data for a tissue magnetic biomarker," *Magn Reson Med*, vol. 73, no. 1, pp. 82-101, Jan 2015.
- [5] J. Acosta-Cabronero et al., "The whole-brain pattern of magnetic susceptibility perturbations in Parkinson's disease," *Brain*, vol. 140, no. 1, pp. 118-131, Jan 2017.
- [6] J. Acosta-Cabronero, G. B. Williams, A. Cardenas-Blanco, R. J. Arnold, V. Lupson, and P. J. Nestor, "In vivo quantitative susceptibility mapping (QSM) in Alzheimer's disease," *PLoS One*, vol. 8, no. 11, p. e81093, 2013.
- [7] S. Ayton et al., "Cerebral quantitative susceptibility mapping predicts amyloid-beta-related cognitive decline," *Brain*, vol. 140, no. 8, pp. 2112-2119, Aug 2017.
- [8] A. Deistung, F. Schweser, and J. R. Reichenbach, "Overview of quantitative susceptibility mapping," *NMR Biomed*, vol. 30, no. 4, Apr 2017.
- [9] A. M. Elkady, D. Cobzas, H. Sun, G. Blevins, and A. H. Wilman, "Discriminative analysis of regional evolution of iron and myelin/calcium in deep gray matter of multiple sclerosis and healthy subjects," *J Magn Reson Imaging*, Mar 2018.
- [10] C. Langkammer, L. Pirpamer, S. Seiler, A. Deistung, F. Schweser, S. Franthal, N. Homayoon, P. Katschnig-Winter, M. Koegl-Wallner, T. Pendl et al., "Quantitative susceptibility mapping in Parkinson's disease," *PLoS One*, vol. 11, no. 9, e0162460, 2016.
- [11] H. Sun, A. J. Walsh, R. M. Lebel, G. Blevins, I. Catz, J. Lu, E. S. Johnson, D. Emery, K. Warren, and A. Wilman, "Validation of quantitative susceptibility mapping with Perls' iron staining for subcortical gray matter," *Neuroimage*, vol. 105, pp. 486-492, 2015.
- [12] M. Juhás, H. Sun, M. Brown, M. MacKay, K. Mann, W. Sommer, A. Wilman, S. Dursun, and A. Greenshaw, "Deep grey matter iron accumulation in alcohol use disorder," *NeuroImage*, vol. 148, pp. 115-122, 2017.
- [13] B. Bilgic, A. Pfefferbaum, T. Rohlfing, E. V. Sullivan, and E. J. N. Adalsteinsson, "MRI estimates of brain iron concentration in normal aging using quantitative susceptibility mapping," *NeuroImage*, vol. 59, no. 3, pp. 2625-2635, 2012.
- [14] L. Chen, A. Soldan, K. Oishi et al., "Quantitative susceptibility mapping of brain iron and β -amyloid in MRI and PET relating to cognitive performance in cognitively normal older adults," *Radiology*, vol. 298, no. 2, pp. 353-362, 2021.
- [15] S. Treit, N. Naji, P. Seres, J. Rickard, E. Stolz, A. Wilman, and C. Beaulieu, "R2* and quantitative susceptibility mapping in deep gray matter of 498 healthy controls from 5 to 90 years," *Human Brain Mapping*, vol. 42, no. 14, pp. 4597-4610, 2021.
- [16] T. Kunieda et al., "Estimation of Amyloid- β Positivity Using QSM Images Considering Age Information," in *Proc. 2023 Int. Conf. Consumer Electronics-Taiwan (ICCE-Taiwan)*, 2023, pp. 165-166.
- [17] C. B. Poynton, M. Jenkinson, E. Adalsteinsson, E. V. Sullivan, A. Pfefferbaum, and W. Wells, 3rd, "Quantitative susceptibility mapping by inversion of a perturbation field model: correlation with brain iron in normal aging," *IEEE Trans Med Imaging*, vol. 34, no. 1, pp. 339-53, Jan 2015.
- [18] A. De, H. Sun, D. J. Emery, K. S. Butcher, and A. H. Wilman, "Rapid quantitative susceptibility mapping of intracerebral hemorrhage," *Journal of Magnetic Resonance Imaging*, vol. 51, no. 3, pp. 712-718, 2020.
- [19] H. Sun, A. C. Klahr, M. Kate, L. C. Gioia, D. J. Emery, K. S. Butcher, and A. H. Wilman, "Quantitative susceptibility mapping for following intracranial hemorrhage," *Radiology*, vol. 288, no. 3, pp. 830-839, 2018.
- [20] S. Wang, M. Lou, T. Liu, D. Cui, X. Chen, and Y. Wang, "Hematoma volume measurement in gradient echo MRI using quantitative susceptibility mapping," *Stroke*, vol. 44, no. 8, pp. 2315-7, Aug 2013.
- [21] D. Z. Balla, R. M. Sanchez-Panchuelo, S. J. Wharton, G. E. Hagberg, K. Scheffler, S. T. Francis, and R. Bowtell, "Functional quantitative susceptibility mapping (fQSM)," *Neuroimage*, vol. 100, pp. 112-124, 2014.
- [22] Y. Ma, H. Sun, J. Cho, E. L. Mazerolle, Y. Wang, and G. B. Pike, "Cerebral OEF quantification: A comparison study between quantitative susceptibility mapping and dual-gas calibrated BOLD imaging," *Magnetic Resonance in Medicine*, vol. 83, no. 1, pp. 68-82, 2020.
- [23] H. Sun, P. Seres, and A. H. Wilman, "Structural and functional quantitative susceptibility mapping from standard fMRI studies," *NMR in Biomedicine*, vol. 30, no. 4, e3619, 2017.
- [24] T. Liu, P. Spincemaille, L. de Rochefort, B. Kressler, and Y. Wang, "Calculation of susceptibility through multiple orientation sampling (COSMOS): A method for conditioning the inverse problem from measured magnetic field map to susceptibility source image in MRI," *Magnetic Resonance in Medicine*, vol. 61, no. 1, pp. 196-204, 2008.
- [25] K. Shmueli, J. A. de Zwart, P. van Gelderen, T. Q. Li, S. J. Dodd, and J. H. Duyn, "Magnetic susceptibility mapping of brain tissue in vivo using MRI phase data," *Magn Reson Med*, vol. 62, no. 6, pp. 1510-22, Dec 2009.

- [26] W. Li et al., "A method for estimating and removing streaking artifacts in quantitative susceptibility mapping," *Neuroimage*, vol. 108, pp. 111-22, Mar 2015.
- [27] J. Liu et al., "Morphology enabled dipole inversion for quantitative susceptibility mapping using structural consistency between the magnitude image and the susceptibility map," *Neuroimage*, vol. 59, no. 3, pp. 2560-8, Feb 2012.
- [28] T. Liu, W. Xu, P. Spincemaille, A. S. Avestimehr, and Y. Wang, "Accuracy of the morphology enabled dipole inversion (MEDI) algorithm for quantitative susceptibility mapping in MRI," *IEEE Trans Med Imaging*, vol. 31, no. 3, pp. 816-24, Mar 2012.
- [29] L. Bao, X. Li, C. Cai, Z. Chen, and P. C. M. van Zijl, "Quantitative Susceptibility Mapping Using Structural Feature Based Collaborative Reconstruction(SFCR) in the Human Brain," *IEEE Transactions on Medical Imaging*, vol. 35, no. 9, pp. 2040-2050, 2016.
- [30] H. Wei et al., "Streaking artifact reduction for quantitative susceptibility mapping of sources with large dynamic range," *NMR in Biomedicine*, vol. 28, no. 10, pp. 1294-1303, 2015.
- [31] H. Sun, Y. Ma, M. E. MacDonald, and G. B. Pike, "Whole head quantitative susceptibility mapping using a least-norm direct dipole inversion method," *Neuroimage*, vol. 179, pp. 166-175, Oct 2018.
- [32] J. Yoon et al., "Quantitative susceptibility mapping using deep neural network: QSMnet," *Neuroimage*, vol. 179, pp. 199-206, Oct 2018.
- [33] W. Jung et al., "Exploring linearity of deep neural network trained QSM: QSMnet+," *Neuroimage*, vol. 211, p. 116619, May 2020.
- [34] Y. Chen, A. Jakary, S. Avadiappan, C. P. Hess, and J. M. Lupo, "QSMGAN: Improved Quantitative Susceptibility Mapping using 3D Generative Adversarial Networks with increased receptive field," *Neuroimage*, vol. 207, p. 116389, Feb 2020.
- [35] K.-W. Lai, M. Aggarwal, P. van Zijl, X. Li, and J. Sulam, "Learned Proximal Networks for Quantitative Susceptibility Mapping," *Cham*, 2020, pp. 125-135: Springer International Publishing.
- [36] Z. Lu et al., "S2Q-Net: Mining the High-Pass Filtered Phase Data in Susceptibility Weighted Imaging for Quantitative Susceptibility Mapping," *IEEE J Biomed Health Inform*, vol. 26, no. 8, pp. 3938-3949, Aug 2022.
- [37] R. Feng et al., "MoDL-QSM: Model-based deep learning for quantitative susceptibility mapping," *Neuroimage*, vol. 240, p. 118376, Oct 2021.
- [38] S. Bollmann et al., "DeepQSM - using deep learning to solve the dipole inversion for quantitative susceptibility mapping," *Neuroimage*, vol. 195, pp. 373-383, Jul 2019.
- [39] Y. Gao et al., "xQSM: quantitative susceptibility mapping with octave convolutional and noise-regularized neural networks," *NMR Biomed*, vol. 34, no. 3, p. e4461, Mar 2021.
- [40] L. Bao, H. Zhang, and Z. Liao, "A spatially adaptive regularization based three-dimensional reconstruction network for quantitative susceptibility mapping," *Physics in Medicine & Biology*, vol. 69, no. 4, 045030, 2024.
- [41] Z. Xiong, Y. Gao, F. Liu, and H. Sun, "Affine transformation edited and refined deep neural network for quantitative susceptibility mapping," *Neuroimage*, vol. 267, p. 119842, Feb 2023.
- [42] Z. Xiong, Y. Gao, Y. Liu, A. Fazlollahi, P. Nestor, F. Liu, and H. Sun, "Quantitative susceptibility mapping through model-based deep image prior (MoDIP)," *NeuroImage*, vol. 291, 120583, 2024.
- [43] G. Oh, H. Bae, H. S. Ahn, S. H. Park, W. J. Moon, and J. C. Ye, "Unsupervised resolution-agnostic quantitative susceptibility mapping using adaptive instance normalization," *Med Image Anal*, vol. 79, p. 102477, Jul 2022.
- [44] H. Wei et al., "Learning-based single-step quantitative susceptibility mapping reconstruction without brain extraction," *Neuroimage*, vol. 202, p. 116064, Nov 2019.
- [45] Y. Gao et al., "Instant tissue field and magnetic susceptibility mapping from MRI raw phase using Laplacian enhanced deep neural networks," *Neuroimage*, vol. 259, p. 119410, Oct 2022.
- [46] Y. Gao et al., "Plug-and-Play latent feature editing for orientation-adaptive quantitative susceptibility mapping neural networks," *Med Image Anal*, vol. 94, p. 103160, May 2024.
- [47] K. M. Koch, X. Papademetris, D. L. Rothman, and R. A. de Graaf, "Rapid calculations of susceptibility-induced magnetostatic field perturbations for in vivo magnetic resonance," *Phys Med Biol*, vol. 51, no. 24, pp. 6381-402, Dec 2006.
- [48] J. P. Marques and R. Bowtell, "Application of a Fourier-based method for rapid calculation of field inhomogeneity due to spatial variation of magnetic susceptibility," *Concepts in Magnetic Resonance Part B: Magnetic Resonance Engineering*, vol. 25B, no. 1, pp. 65-78, 2005.
- [49] M. Z. Alom, M. Hasan, C. Yakopcic, T. M. Taha, and V. K. Asari, "Recurrent residual convolutional neural network based on u-net (r2u-net) for medical image segmentation," *arXiv preprint arXiv:1802.06955*, 2018.
- [50] W. Wang, K. Yu, J. Hugonot, P. Fua, and M. Salzmann, "Recurrent U-Net for resource-constrained segmentation," in *Proceedings of the IEEE/CVF international conference on computer vision*, 2019, pp. 2142-2151.
- [51] A. Sherstinsky, "Fundamentals of recurrent neural network (RNN) and long short-term memory (LSTM) network," *Physica D: Nonlinear Phenomena*, vol. 404, 132306, 2020.
- [52] H. S. Abdul-Rahman, M. A. Gdeisat, D. R. Burton, M. J. Lalor, F. Lilley, and C. J. Moore, "Fast and robust three-dimensional best path phase unwrapping algorithm," *Applied Optics*, vol. 46, no. 26, pp. 6623-6635, 2007.
- [53] H. Sun and A. H. Wilman, "Background field removal using spherical mean value filtering and Tikhonov regularization," *Magnetic Resonance in Medicine*, vol. 71, no. 3, pp. 1151-1157, 2014.
- [54] Q. C. O. Committee et al., "QSM reconstruction challenge 2.0: design and report of results," vol. 86, no. 3, pp. 1241-1255, 2021.
- [55] W. Jung, S. Bollmann, and J. Lee, "Overview of quantitative susceptibility mapping using deep learning: Current status, challenges and opportunities," *NMR in Biomedicine*, vol. 35, no. 4, e4292, 2022.
- [56] G. E. Hinton, N. Srivastava, A. Krizhevsky, I. Sutskever, and R. R. Salakhutdinov, "Improving neural networks by preventing co-adaptation of feature detectors," *arXiv preprint arXiv:1207.0580*, 2012.
- [57] N. Srivastava, G. Hinton, A. Krizhevsky, I. Sutskever, and R. Salakhutdinov, "Dropout: a simple way to prevent neural networks from overfitting," *The Journal of Machine Learning Research*, vol. 15, no. 1, pp. 1929-1958, 2014.